Volume 1 | Number 1 | Jan 2013 | Pages 1–100

Journal of
Materials Chemistry A

Materials for energy and sustainability
www.rsc.org/materialsA

Li⁺

ROYAL SOCIETY
OF CHEMISTRY

ROYAL SOCIETY
OF CHEMISTRY

www.rsc.org/materialsA

Journal Name

ARTICLE

Biomass-mediated synthesis of carbon-supported nanostructured metal sulfides for ultra-high performance lithium-ion batteries

Y. Lu [a] and E. Fong* [a]

A bio-inspired, environmentally friendly route to prepare three-dimensional (3D) hybrid nanostructured materials for lithium-ion batteries (LIBs) is presented. Alginate, a naturally occurring biopolymer, was employed as a template to synthesize molybdenum sulfide (MoS_2) nanostructures from ammonium heptamolybdate and L-cysteine precursors under physiological conditions. Here we show that MoS_2 precursors did not interact specifically with alginate; instead, MoS_2 nanocrystallites were precipitated within a porous alginate matrix made up of hollow nanospheres. In contrast, when cobalt (Co^{2+}) was added to crosslink alginate mixed with ammonium heptamolybdate and L-cysteine precursors, a highly crosslinked hydrogel network was obtained instead. Upon annealing, $CoMoS_{3.13}$ nanocrystallites were found to be well-dispersed within a 3D porous carbon matrix ($CoMoS_{3.13}$@ADC, ADC represents alginate derived carbon). The novel $CoMoS_{3.13}$@ADC hybrid materials were evaluated as anodes in lithium ion batteries, and were found to have exceptional capability performance, excellent cycle stability and rate performance. The lithiation mechanisms of $CoMoS_{3.13}$@ADC were proposed; the shortened ion transport paths and rapid reaction kinetics were due to the nano-sized $CoMoS_{3.13}$ crystals and inter-connected 3D pore structure. In summary, we showed that alginate biopolymers could offer a facile route towards the synthesis of novel 3D metal sulfides hybrid nanomaterials for energy storage applications.

Introduction

There is a need to engineer advanced nanomaterials for electrodes in lithium-ion batteries (LIBs), especially for next-generation, high-power applications (e.g., portable electronics, storage of renewable energy, electric vehicles and smart grids). Metal sulfides are promising materials as both cathodes and anodes in high-energy LIBs[1, 2]. In recent years, layered transition metal sulfides of MS_x (M = Mo, W, V, Sn, Zr) have attracted great attention due to their structure peculiarities, redox variabilities and higher cycling stabilities[3-7]. Amongst the metal sulfides, MoS_2 has the highest lithium storage capacity (669 mA h g^{-1}). Yet, practical applications of MoS_2 as anode materials are challenging due its low intrinsic electric conductivity and large volume changes during the lithium insertion and extraction process. As a result, there is dramatic electrode pulverization and severe loss of electrical contact from the current collector, leading to poor cyclability and sluggish dynamics of MoS_2 for lithium storage.[4, 8-10]

In order to increase the performance of metal sulfides, various strategies have been investigated, including preparing MoS_2 nanostructures with diverse morphologies or coupling MoS_2 with electrically conductive polymer or carbon to construct nanocomposites.[11-13] There have been efforts to increase the electrode performances in batteries by increasing the contact areas between the active materials and the electrolyte; either by reducing the size of the active material to the nanoscale, or by introducing porosity to increase the overall surface area of the electrode. Both strategies have been found to shorten both electronic and ionic pathways within particles according to $t \approx L^2/D$ (t: characteristic time constant; D: ion diffusivity; L: diffusion length). In particular, mesopores and macropores have been found to facilitate ion lithiation and ion transport respectively; both features are essential for achieving ultra-high performances in LIBs.

Bio-inspired synthesis or biotemplating routes offer a tailorable and environmental friendly alternative to produce 3D electrode nanomaterials with high performance for LIBs. Due to their mild synthesis conditions[14, 15], a variety of inorganic/carbon materials have been prepared from biological precursors. For example, MnO/C microspheres have been successfully synthesized from microalgae,[16] TaC/activated carbon microfibers from bamboo,[17] B_4C/carbon microfibers from cotton,[18] as well as $FePO_4$/C from peptides[19]. Likewise, we have previously developed novel 3D carbon foams containing metal vanadium phosphates ultrafast battery cathodes using elastin-like polypeptide templates.[20]

Notably, biopolymers derived from biomass are attractive raw materials for the preparation of hierarchically hybrid materials. In particular, alginate, a widely abundant polyssacharide extracted from algae, has been widely used in tissue engineering and drug delivery. Alginates are known to associate with divalent cations

[a.] School of Materials Science and Engineering, Nanyang Technological University, 639798, Singapore E-mail: wmfong@ntu.edu.sg
† Footnotes relating to the title and/or authors should appear here.
Electronic Supplementary Information (ESI) available: [details of any supplementary information available should be included here]. See DOI: 10.1039/x0xx00000x

such as Ca^{2+} to form hydrogel networks via the "egg-box" model.[21-24] Many have successfully demonstrated the use of such crosslinked alginate scaffolds to prepare porous carbons[25-27], metal nanostructures (Au, Ag, Co, and Ni nanoparticles and Te nanowires)[28] and metal oxides ($YBa_2Cu_4O_8$ and $La_{0.67}Sr_{0.33}MnO_3$)[23] as well as metal/metal oxide nanocomposites (Au/CeO_2)[29].

Since alginate is relatively abundant in nature, it is highly attractive to exploit alginate as a low cost, scalable template for the synthesis of active materials for energy storage. Moreover, there have been no attempts made to prepare other active nanomaterial with complex stoichiometric chemistries using alginate-assisted routes. In this work, we explored the synthesis of metal sulfides using alginate as a carbon precursor and template. The synthesis strategy used in this work is outlined in **Scheme 1**. L-cysteine was used as source of sulfur due to its environmentally benign properties and the presence of several functional groups (-SH,-NH_2, and $-COO^-$), which can aid the formation of two-dimensional structures for the resulting compounds.[30-33] Here, ammonium heptamolybdate tetrahydrate (($NH_4)_6Mo_7O_{24} \cdot 4H_2O$) precursors were mixed homogeneously with sodium alginate and L-cysteine at room temperature and freeze-dried. After annealing, MoS_2 nanocrystals were found dispersed within a porous carbon matrix, primarily made up of carbon nanoshells (MoS_2@ADC; ADC represents alginate derived carbons). Separately, when the mixture of alginate and MoS_2 precursors were added to divalent cations (i.e., Co^{2+}) solution, a highly crosslinked hydrogel network was obtained. Well-crystallized $CoMoS_{3.13}$ nanocrystals were found embedded within a porous carbon matrix ($CoMoS_{3.13}$@ADC) after annealing the above hydrogel. Both as-annealed materials exhibited ultra-high performances when tested as anodes for LIBs, highlighting the potential of alginates for the synthesis of complex metal sulfide nanomaterials for high performance LIBs.
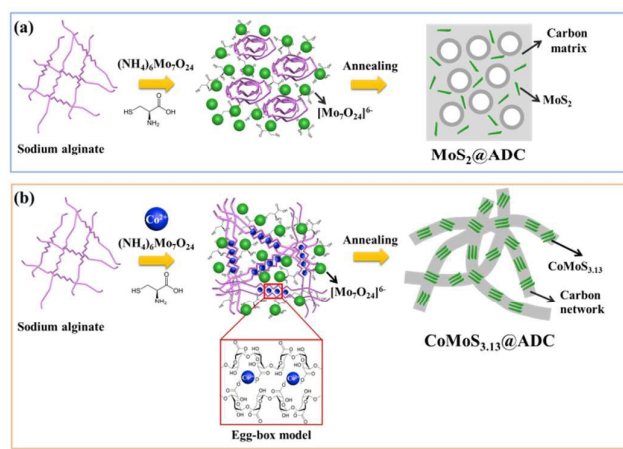
Scheme 1. Schematic illustrating the formation of (a) MoS_2@ADC and (b) $CoMoS_{3.13}$@ADC using sodium alginate.

Experimental

Materials

Ammonium heptamolybdate tetrahydrate (($NH_4)_6Mo_7O_{24} \cdot 4H_2O$, Alfa Aesar), L-cysteine ($C_3H_7NO_2S$, Sigma-Aldrich), Cobalt nitrate hexahydrate ($Co(NO_3)_2 \cdot 6H_2O$, Sigma-Aldrich) and sodium alginate (($C_6H_7O_6Na)_n$, Spectrum) were purchased and used without further treatment.

Synthesis of MoS_2@ADC and $CoMoS_{3.13}$ @ADC

Sodium alginate (2g) was dissolved in ddH_2O (90 mL) at 80°C to achieve a homogeneous solution. Next, sodium alginate was mixed with 1M L-cysteine in 1:1 volume ratio, and stirred continuously at room temperature for 1 h. The mixture (4 ml) was then added to 1 ml of ammonium heptamolybdate tetrahydrate (($NH_4)_6Mo_7O_{24} \cdot 4H_2O$; 0.143 M) and thoroughly mixed for 1 h. The mixture was then frozen at -80°C and lyophilized. The lyophilized sample was subsequently annealed at 800°C for 2 h, with a heating rate of 4 °C min^{-1} in argon atmosphere. The as-annealed sample is referred to as MoS_2@ADC in this work.

The same procedure was employed to obtain $CoMoS_{3.13}$@ADC, except with some modifications. First, sodium alginate, L-cysteine and ($NH_4)_6Mo_7O_{24} \cdot 4H_2O$ were mixed in the same way as in the case of MoS_2@ADC. The mixture (6 ml) was then added to 15 ml of cobalt nitrate hexahydrate ($Co(NO_3)_2 \cdot 6H_2O$, 1 M). The solution was kept stagnant at 4°C for 1h to allow complete gelation of alginate. Subsequently, the treated hydrogel was washed several times with ddH_2O, before freezing at -80°C and lyophilized. The resulting sample was annealed at 600°C for 2 h, with a heating rate of 4 °C min^{-1} in argon atmosphere. The as-annealed sample is referred to as $CoMoS_{3.13}$ @ADC in this work.

Materials characterization

The morphologies of the prepared materials were examined by field emission scanning electron microscope (FESEM, JEOL 7600F) and transmission electron microscopy (TEM, JEOL 2100F) operated at an accelerating voltage of 200 kV. Powder X-ray diffraction (XRD, Shimadzu powder, 40 kV/30 mA, Cu-Ka radiation) was employed to identify the crystalline phases of the synthesized materials. The nitrogen adsorption–desorption isotherms was acquired using an ASAP Tri-star II 3020 analyzer, and the specific surface area was calculated using the Brunauer–Emmett–Teller (BET) method. The pore size distribution was derived from the desorption branch of the isotherm using the Barrett–Joyner–Halenda (BJH) method. Thermogravimetric analysis (TGA) was performed using TA Instrument Q500. The chemical composition was analysed by energy dispersive X-ray spectroscopy (EDS) instrument attached to the JEOL-2100F microscope.

Electrochemical Measurements

The as-prepared materials were evaluated as anodes using a coin cell assembly. The coin cells were assembled in an argon-filled glovebox with both moisture and oxygen levels less than 1 ppm. The electrodes were prepared by mixing 80 wt % MoS_2@ADC or $CoMoS_{3.13}$@ADC with carbon black (10 wt %) and polyvinylidene fluoride (PVDF, 10 wt %) in n-methyl-2-pyrrolidone solvent and then pasted onto the copper foil substrate, and dried in a vacuum oven at 80°C for 2 days. High-purity lithium foil was used as counter and reference electrodes. Celgard 2400 was used as a separator, with

lithium foil as the counter electrode, and 1 mol L^{-1} LiPF$_6$ solution in a mixed solvent of ethylene carbonate (EC) and diethyl carbonate (DEC) (v/v = 1 : 1) served as the electrolyte. Cyclic voltammetry (CV) was measured using an electrochemical workstation (CHI614b, China). Galvanostatic charge–discharge measurements of the prepared anodes versus Li/Li$^+$ were performed at room temperature under different rates in a voltage range of 0.01 – 3.0 V on NEWARE multichannel battery test system. All electrochemical tests were performed at room temperature. The typical mass loadings of active materials (MoS$_2$ in MoS$_2$@ADC, CoMoS$_{3.13}$ in CoMoS$_{3.13}$@ADC) of MoS$_2$@ADC anode and CoMoS$_{3.13}$@ADC anode were calculated to be 0.76 mg cm^{-2} and 0.90 mg cm^{-2}, respectively. The specific capacity was calculated based on the prepared active materials.

Results and discussion

Characterization of MoS$_2$@ADC

The as-annealed MoS$_2$@ADC samples were subjected to electron microscopy and XRD characterization. The surface of the as-annealed MoS$_2$@ADC sample appeared to be covered with nanospheres with diameters of about 50 nm (Fig. 1a-b). Under the TEM, these nanospheres were found to be hollow, and consisted mainly of graphitized carbon (Fig. 1c-d). Further analysis of the hollow nanospheres (or nanoshells) revealed lattice spacing of about 0.367 nm, consistent with previous report on graphitized carbon (Fig 1d).[34] There also exists unstructured carbon matrix surrounding the hollow nanoshells. Here, MoS$_2$ nanocrystals were found heterogeneously scattered within the matrix (Fig. 1e). Inset in The lattice spacings of the MoS$_2$ nanocrystals were measured to be 0.62 nm, corresponding to the (002) plane of MoS$_2$ (Fig. 1e). XRD further confirmed the presence of hexagonal MoS$_2$ (JCPDS card No. 37-1492; Fig. 1f). The (002) peak was notably absent, which suggests that the MoS$_2$ in the as-prepared MoS$_2$@ADC consist of single or several layers.[3, 13, 35, 36] The broadened nature of the spectrum further indicated that the MoS$_2$ obtained in this work were not well-crystalized. Using the Scherrer's equation, the estimated grain size for MoS$_2$ was around 3.6 nm, which was consistent with the thickness of the observed layered MoS$_2$ nanostructure in Fig. 1e, further confirming its few-layered characteristic.

Formation of alginate nanoshells are typically facilitated by the addition of divalent cations such as Ca^{2+} or oil-in-water emulsification[37-39]. The nanoshells observed here are also significantly smaller than the ones reported in the literature (>100nm).[40] To investigate possible mechanisms for the formation of the nanoshells, alginate and alginate/L-cysteine mixtures were separately freeze-dried and annealed as controls. In the case of alginate only, we did not observe the formation of hollow carbon shells (Fig. S1a,c). In the control where L-cysteine has been added to alginate, a highly porous structure was obtained (Fig. S1b,d). However, at higher magnifications, the pores were found to be significantly larger than those found in MoS$_2$@ADC. These larger pores could be due to the evaporation of sulfur liquid droplets[41] generated during the pyrolysis of L-cysteine.[41] Hence, we conclude that both alginate and L-cysteine did not contribute to the formation of the carbon nanoshells found in MoS$_2$@ADC. Hence, it is likely that there exist electrostatic interactions between anionic alginate and the NH$_4^+$ ions dissociated from the Mo precursors. These interactions drive the self-assembly of micellar structures, which further grow during the annealing process, controlled by diffusion or carbonization reaction according to the theory of Ostwald ripening.[42]
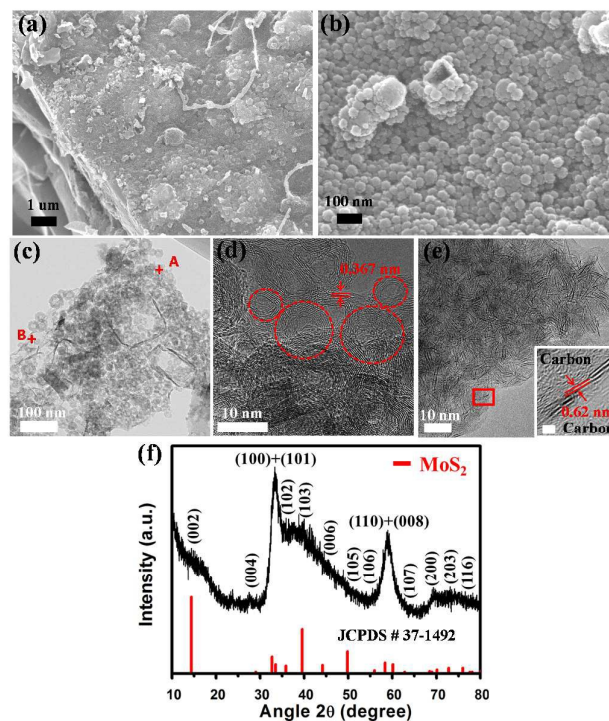

Fig. 1. (a,b) SEM images and (c-e) TEM images of MoS$_2$@ADC. Images at points A and B in (c) are shown in (d) and (e) respectively. Inset in (e) is a high magnification of the area enclosed by the red box (scale bar: 2 nm). (f) XRD spectrum of MoS$_2$@ADC.

Interestingly, MoS$_2$ crystals can only be found in areas surrounding the graphitized carbon nanoshells. We also did not notice any MoS$_2$ crystals embedded within the walls of the carbon nanoshells. This suggested that the molybdate (Mo$_7$O$_{24}$)$^{6-}$ ions did not interact specifically with alginate, but react with the L-cysteine dispersed within the alginate matrix to form MoS$_2$ nanocrystals.

Characterization of CoMoS$_{3.13}$@ADC

Fig. 2a,b show that CoMoS$_{3.13}$@ADC has similar bead-like surface like that of MoS$_2$@ADC. However, under the TEM, the morphology of CoMoS$_{3.13}$@ADC was strikingly different than that of MoS$_2$@ADC (Fig. 2c). We did not observe any carbon nanoshells. Instead, a porous structure was obtained, within which were aggregates of nanocrystals with lengths of about 25 nm (Fig. 2d). The average lattice spacing of the aggregates were found to be 0.615 nm, corresponding to the lattice spacing of reported CoMoS$_{3.13}$.[43] In

addition, crystal lattices with spacings of 0.168 nm and 0.253 nm were also observed; both lattice spacings too, can be ascribed to $CoMoS_{3.13}$. EDX elemental mapping of $CoMoS_{3.13}$@ADC sample (Fig. S2) showed even dispersion of C, Co, Mo and S elements in the hybrid nanostructure, confirming the presence of carbon matrix. Raman spectrum (Fig. S4) exhibited broaden D band and G band peaks with intensity ratio (I_D/I_G) of 1.06, indicating the carbon has low graphitization degree [44, 45] due to low annealing temperature of 600 ℃.

XRD analysis of $CoMoS_{3.13}$@ADC (Fig. 2f) confirmed the presence of well-crystallized $CoMoS_{3.13}$@ADC, since peaks correspond only to $CoMoS_{3.13}$ (JCPDS card No. 16-0439) [43] but not to pure MoS_2, Co_9S_8 phase or their simple mixtures. Using the Scherrer's equation, the estimated grain sizes of $CoMoS_{3.13}$ were 4.0 nm and 16.8 nm, which corresponded to the thickness and the length of $CoMoS_{3.13}$ nanocrystals observed in TEM images (Fig. 2d,e) respectively. Although $CoMoS_x$ have been historically used as a hydrodesulfurization catalyst,[46-48] application of $CoMoS_x$ as LIBs electrodes have not been reported.
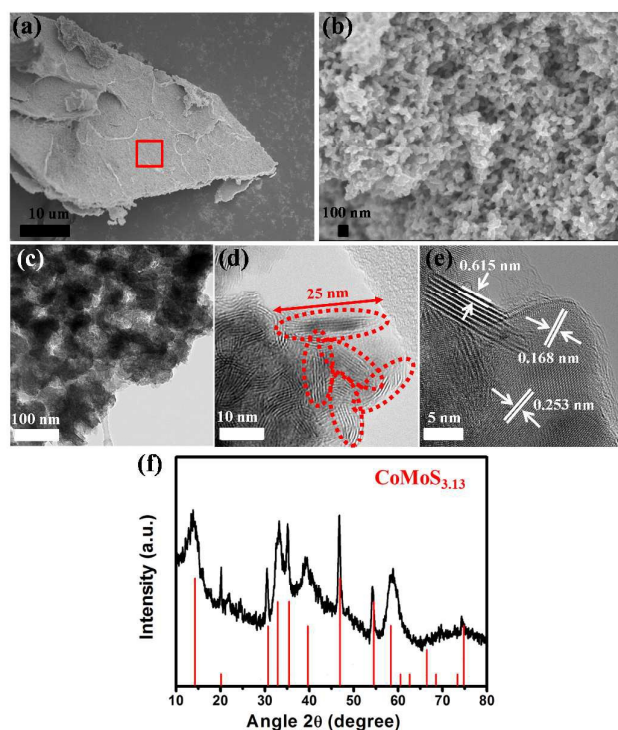

Fig. 2. (a,b) SEM images of $CoMoS_{3.13}$@ADC. (b) Image showing a magnified view of the area enclosed by red box in (a). (c-e) TEM images and (f) XRD spectrum of $CoMoS_{3.13}$@ADC.

We were able to obtain higher degree of crystallinity in $CoMoS_{3.13}$@ADC, compared to MoS_2@ADC, even under a lower annealing temperature (600 °C). A plausible reason for the higher crystallinity in the $CoMoS_{3.13}$@ADC sample is the presence of cobalt. Addition of cobalt nitrate ($Co(NO_3)_2·6H_2O$) was expected to trigger the gelation of alginate via the well-known "egg-box" model

[21-24, 28] (Scheme 1). The positively-charged Co^{2+} ions are uniformly dispersed throughout the alginate matrix to serve as nucleation sites for subsequent recruitment of molybdate ions. As a result, the molybdate ions associate with the positively charged Co^{2+}, and are consequently immobilized within the alginate hydrogel matrix together with the cysteine. The close proximity between Co^{2+}, molybdate ions and sulfur from the L-cysteine facilitates the formation of well-crystallized $CoMoS_{3.13}$ nanocrystals during annealing, despite a low annealing temperature of 600°C. In the annealing step, the alginate matrix further decomposed into carbon, providing a highly conductive carbon matrix. Hence, cobalt, together with alginate, played an important role to disperse the $CoMoS_{3.13}$ nanocrystals and reduce the energy barrier for crystal nucleation and growth.

To determine the degree of porosity in the prepared materials, nitrogen adsorption and desorption measurements were taken. For MoS_2@ADC sample, the BET specific surface area was calculated to be 187.7 m^2 g^{-1} by the desorption branch. However, for $CoMoS_{3.13}$@ADC, the BET specific surface area was only 55 m^2 g^{-1}. One possible reason for the larger surface areas in MoS_2@ADC, could be the presence of carbon nanoshells, that were absent in $CoMoS_{3.13}$@ADC. The wide pore size distribution for MoS_2@ADC (inset of Fig.S3 a) may hence be attributed to the broad sizes of the carbon nanoshells as observed in Fig. 1c. While for $CoMoS_{3.13}$@ADC, a broaden peak around 20~30 nm is observed (inset of Fig.S3b), indicating the mesoporous feature of the pores, which can be also observed from the typical IV-type shaped nitrogen adsorption-desorption isothermal curves in Fig. S3b. Finally, thermogravimetric analysis was employed to determine the content of active materials present in the samples. The contents of MoS_2 and $CoMoS_{3.13}$ in the corresponding hybrid materials were calculated to be 63% and 75% respectively (Fig. S3c-d). The residual masses were assumed to be MoO_3 and Co_3O_4 respectively at 800°C due to the oxidation of the active materials (MoS_2 and $CoMoS_{3.13}$) in air.

Lithium storage mechanism and electrochemical performance

The electrochemical properties of MoS_2@ADC and $CoMoS_{3.13}$@ADC were investigated as anodes in LIBs. Fig. 3a shows the cyclic voltammetry (CV) curve of MoS_2@ADC. The CV behaviour of our MoS_2@ADC is generally consistent with those previously reported MoS_2 materials.[30, 49, 50]

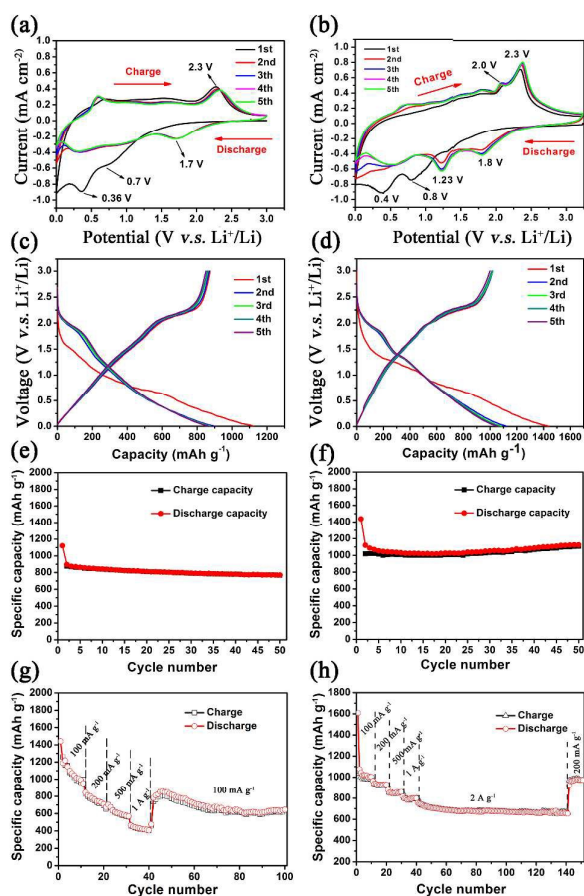Fig. 3. CV curves of MoS$_2$@ADC (a) and CoMoS$_{3.13}$@ADC (b) electrodes at a scanning rate of 0.5 mV s^{-1} during the initial five cycles; The first five galvanostatic discharge/charge profiles of MoS$_2$@ADC (c), CoMoS$_{3.13}$@ADC (d) electrodes at 100 mA g^{-1}; cycle performance of MoS$_2$@ADC (e), CoMoS$_{3.13}$@ADC (f) electrodes at 100 mA g^{-1}; rate performance of MoS$_2$@ADC (g), CoMoS$_{3.13}$@ADC (h) electrodes.
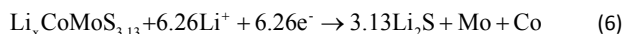
In the first cathodic sweep, the peak at 0.7 V is attributed to the intercalation of lithium ions into the MoS$_2$ lattice which transforms the triangular prism (coordination of Mo by six S atoms) into an octahedral structure.[51, 52] The peak at 0.36 V is attributed to the complete reduction of Mo^{4+} to Mo^0 metal, which is followed by the formation of Li$_2$S and a gel-like polymeric layer resulting from electrochemically driven electrolyte degradation.[4] The whole discharge (lithiation) reaction can be expressed as a two-step process based on the following reactions (Equations 1 and 2):

$$MoS_2 + xLi^+ + xe^- \rightarrow Li_xMoS_2 \quad (1)$$

$$Li_xMoS_2 + 4Li^+ + 4e^- \rightarrow 2Li_2S + Mo \quad (2)$$
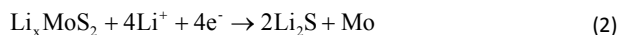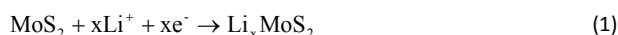
During the first anodic scan, we observed a peak at 2.3 V attributed to the formation of MoS$_2$[4]. Some reports also suggested that this peak is corresponding to the oxidation of Li$_2$S into sulfur.[53, 54] The delithiation process can be expressed as follows:

$$Li_2S + Mo \rightarrow MoS_2 + 4Li^+ + 4e^- \quad (3)$$

$$Li_2S \rightarrow S + 2Li^+ + 2e^- \quad (4)$$
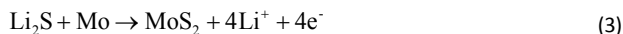
While the lithium storage mechanisms for MoS$_2$ anodes in LIBs are well understood, lithiation mechanisms for CoMoS$_x$ have not been reported. Likewise, reports on transition metal doping in MoS$_2$ and their performances as anodes in LIBs are limited[55], even though doping is known to improve the performance of many electrode materials.[56-61] From the CV curves of CoMoS$_{3.13}$@ADC (Fig. 3b), two obvious peaks were observed in the first catholic scan, which can be a result of a conversion reaction mechanism, found commonly in metal sulfides.[62] The catholic at 0.8 V can be attributed to the insertion of lithium ions into the CoMoS$_{3.13}$ lattice to form Li$_x$CoMoS$_{3.13}$, while the peak at 0.4 V corresponds to the complete reduction of Co^{2+} to Co^0, Mo^{4+} to Mo^0 metal and formation of Li$_2$S. The entire possible discharge (lithiation) reaction is proposed a two-step process based on the following reactions (Equations 5 and 6):

$$CoMoS_{3.13} + xLi^+ + xe^- \rightarrow Li_xCoMoS_{3.13} \quad (5)$$

$$Li_xCoMoS_{3.13} + 6.26Li^+ + 6.26e^- \rightarrow 3.13Li_2S + Mo + Co \quad (6)$$

In the anodic scan for CoMoS$_{3.13}$@ADC, we observed one obvious peak at 2.3 V and another weaker peak at 2.0 V. The peak at 2.3 V is likely contributed by the reversible formation of MoS$_2$, while the weaker peak at 2.0 V is speculated to be due to the formation of cobalt sulfides (CoS$_x$).[63] Herein, the delithiated process of CoMoS$_{3.13}$@ADC electrode can be expressed as following:

$$Li_2S + Mo \rightarrow MoS_2 + 4Li^+ + 4e^- \quad (7)$$

$$xLi_2S + Co \rightarrow CoS_x + 2xLi^+ + 2xe^- \quad (8)$$
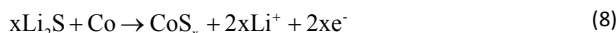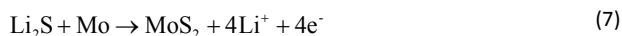
During subsequent cathodic sweeps, the reduction peaks are quite different from the first sweep, and new peaks at 1.7 V for MoS$_2$@ADC (1.8 V and 1.23 V for CoMoS$_{3.13}$@ADC) were observed, which is due to lithium intercalation on different defect sites of electrode active materials (MoS$_2$ for MoS$_2$@ADC and MoS$_2$, CoS$_x$ for CoMoS$_{3.13}$@ADC) developed during the cycling,[3, 64] which is in agreement with previous observation in the literatures.[30, 49, 65]
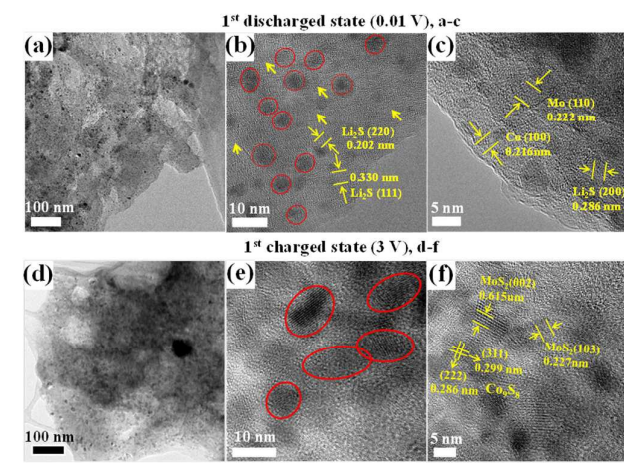
Fig. 4. (a) Representative TEM images for the CoMoS$_{3.13}$ @ACD anode after the first discharged (lithiated) state. (b-c) HRTEM image confirming the generation of Li$_2$S matrix and metallic domains. (d) Representative TEM images for the CoMoS$_{3.13}$ @ACD anode after the first recharged (delithiated) state. (e-f) HRTEM image confirming the regeneration of sulfide nanocrystallites.

We next verify the lithium storage mechanism of CoMoS$_{3.13}$ proposed according to the CV results. The first discharged and charged samples of the CoMoS$_{3.13}$ @ADC electrode were characterized by TEM. Fig. 4a shows a representative TEM image of the CoMoS$_{3.13}$ @ADC electrode upon discharge to 0.01 V. The morphology of CoMoS$_{3.13}$ @ADC was significantly different from the pristine active material (Fig. 2c). The original CoMoS$_{3.13}$ nanocrystals were noticeably absent after the 1st discharge process. Instead, numerous smaller domains (less than 5 nm) with obvious lattice fringes were observed (Fig. 4b). Amongst them, dark crystals with well-defined shapes (circled using red circles in Fig. 4b) could be identified as metallic Mo (0.222 nm; JCPDS: 42-1120) and Co (0.216 nm; JCPDS: 05-0727) respectively (see Fig. 4c). In addition, particles with lower contrast were also found within the surrounding amorphous matrix. The lattice spacing measured from these particles were consistent with the crystallographic planes (220) and (111) (JCPDS: 65-2981) of Li$_2$S (see Fig. 4b). The Li$_2$S phase is less visible than the metallic phase due to the weak scattering of light constituent elements. This observation confirms the conversion reaction mechanism of CoMoS$_{3.13}$ proposed in this work.

When the anode is recharged to 3.0 V, new nanoparticles were generated from breakdown of the original CoMoS$_{3.13}$ nanocrystals (Fig. 4d, circled in red in Fig. 4e). This phenomenon is commonly observed for metal sulfide electrodes.[54, 66] From Fig. 4f, lattice fringes corresponding to MoS$_2$ (0.615 nm, (002); 0.227 nm, (103), 37-1492) and Co$_9$S$_8$ (0.299 nm, (311); 0.286 nm (222), 86-2273) could also observed. MoS$_2$ is commonly obtained after 1st charge process.[4, 54] However, it is surprising to obtain Co$_9$S$_8$ in the charged electrode.
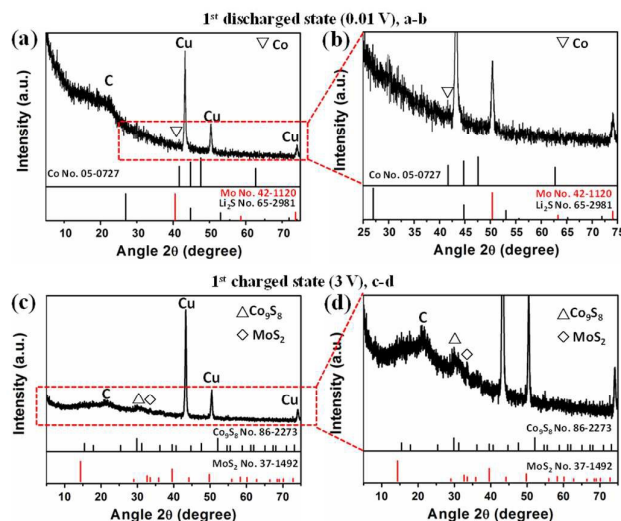

Fig. 5. XRD patterns of the CoMoS$_{3.13}$@ACD anode at the first discharged (lithiated) state (a) and recharged (delithiated) state (c): (b) is an enlarged view of the red box in (a); (d) is an enlarged view of the red box in (c).

To further confirm our TEM observations, X-ray diffraction was used to examine the lithiation-delithiation products of CoMoS$_{3.13}$ electrodes. Fig. 5a showed XRD patterns of the discharged electrode. A broadened peak at around 20~25 ° can be ascribed to the presence of carbon (carbon support or super P added in the electrode preparation process) in the electrode. Fig. 5b shows a magnified image of the region enclosed by the red box. Only one peak centered at 41.7 °, can be identified and assigned to Co ((100) plane; JCPDS no. 05-0727). Other peaks were difficult to index due to the high background signals of Cu as well as the small size of the nanocrystals. In combination with our TEM data, it is likely that Li$_2$S, Mo and Co metals were indeed present in the discharged CoMoS$_{3.13}$@ACD electrode.

Likewise for the charged electrode, the broadened carbon peak centered at peak at 20~25 ° was also present. In addition, another broadened peak centered at around 30° was also observed. The position of the peak matched the overlapping peaks of Co$_9$S$_8$ ((311) and (222) planes; JCPDS no. 86-2273) in Fig. 5d. Coincidentally, both of these planes were also observed under HRTEM in Fig. 4f, confirming the presence of Co$_9$S$_8$ in the charged products. Finally, another obvious peak at 33.5° was also present, corresponding to the well-defined MoS$_2$ (101) plane (JCPDS no. 37-1492). Hence, based on the results of HRTEM and XRD, we determined that both Co$_9$S$_8$ and MoS$_2$ were indeed generated during cycling of the CoMoS$_{3.13}$@ACD electrode.

Next, the electrochemical performances of both MoS$_2$@ADC and CoMoS$_{3.13}$@ADC were also evaluated in LIBs. Fig. 3c and d show galvanostatic charge–discharge curves of MoS$_2$@ADC electrode and CoMoS$_{3.13}$@ADC electrode for the first five cycles. From Fig. 3c, we can see that the MoS$_2$@ADC electrode exhibited a discharge

ARTICLE

capacity over 1100 mAh g^{-1} and a reversible capacity of 874 mAh g^{-1} at the first cycle with inconspicuous potential plateaus compared with the reported pure MoS$_2$.[52] Typical potential plateaus at ~1.2 V (contributed by the formation of Li$_x$MoS$_2$), and at ~0.7 V (contributed to the formation of Mo metal and LiS$_2$)[3, 67, 68] were absent. The missing peaks can be explained by the presence of carbon material within the electrode.[30, 69]

As for CoMoS$_{3.13}$@ADC electrode, an initial discharge capacity of 1436 mAh g^{-1} and an initial charge capacity of 1121 mAh g^{-1} were obtained (Fig. 3d). This result was significantly better than the MoS$_2$@ADC electrode, even comparable to the performance of hybrid materials containing graphene (Table S1).[4, 30, 50] Similar to the MoS$_2$@ADC electrode, there were no obvious potential plateaus observed in the first discharge curve due to the presence of carbon in the hybrid material. However, two potential plateaus around 1.8 V and 1.2 V appeared in the following discharge curves, consistent with the cyclic voltammetry curve (Fig. 3b).

The cycle performances of MoS$_2$@ADC and CoMoS$_{3.13}$@ADC electrodes at 100 mA g^{-1} were also estimated from Fig. 3e and f respectively. The cycle stability of CoMoS$_{3.13}$@ADC electrode was clearly better than MoS$_2$@ADC with a residual capacity of 1125 mAh g^{-1} after 50 cycles. In fact, the cycle performances of CoMoS$_{3.13}$@ADC electrodes are superior than electrodes containing graphene.[30, 50] The CoMoS$_{3.13}$@ADC electrodes also demonstrate good rate capability, as shown in Fig. 3h. Reversible capacities of about 1077 mAh g^{-1} at a discharge-charge rate of 100 mA g^{-1}, 965 mAh g^{-1} at 200 mA g^{-1}, 877 mAh g^{-1} at 500 mA g^{-1}, 801 mAh g^{-1} at 1 A g^{-1}, 755 mAh g^{-1} at 2 A g^{-1} are achieved, respectively. Moreover, when the testing current is regularly returned to low current rate of 200 mA g^{-1}, the discharge capacity is recovered to 986 mAh g^{-1}, which is the same level or even slightly higher than that (965 mAh g^{-1}) of the initial cycles at 200 mA g^{-1}, indicating it exceptional rate capability. The observation is consisted with the previous reports for conversion electrodes [10, 13, 65, 70] A possible explanation for this phenomena is the presence of the 3D carbon supported CoMoS$_{3.13}$ hybrid architecture, which guaranteed the good conductivity of the active materials even after the pulverization process (Fig. 4 a,d). Therefore, even after high rate testing (10 C), a high discharge capacity can be recovered at low current density owning to the enlarged electrode/electrolyte interface area as well as good conductivity.

Despite the lower specific surface area of CoMoS$_{3.13}$@ADC than MoS$_2$@ADC, the CoMoS$_{3.13}$@ADC electrode displayed significantly better electrochemical properties. The enhanced properties could be due to several reasons. First, CoMoS$_{3.13}$ has a higher theoretical specific capacity (752 mAh g^{-1}) than MoS$_2$ (670 mAh g^{-1}). Second, CoMoS$_{3.13}$ nanocrystals are well-dispersed within the alginate matrix, crosslinked by Co^{2+} ions. The alginate matrix decomposes into a 3D conductive carbon matrix that further facilitates electron transport within the material. In addition to the doping effects of Co, reduced lithium-ion pathways resulting from the 3D nanostructure and enlarged contact areas between the active materials and the electrolyte, led to the overall outstanding electrochemical properties of the CoMoS$_{3.13}$@ADC.

Conclusions

In summary, 3D carbon supported metal sulfides were successfully synthesized through a facile, environment friendly and low cost bio-inspired strategy. Alginate, a common biopolymer derived from biomass, was used as a template for the preparation of 3D MoS$_2$@ADC and CoMoS$_{3.13}$@ADC nanostructures. Particularly, the presence of Co^{2+} resulted in gelation of alginate, and homogeneous nucleation of CoMoS$_{3.13}$ nanocrystals within a porous carbon matrix. When the electrochemical performances of both CoMoS$_{3.13}$@ADC and MoS$_2$@ADC are investigated as anodes in LIBs, CoMoS$_{3.13}$@ADC was found to display exceptional capability performance, excellent cycle stability and rate performances. We show that alginate-assisted synthesis is a facile and environmentally friendly strategy that can be extended to prepare a wide variety of metal compounds with advanced electrochemical properties.

Acknowledgements

Notes and references

1. S. W. Kim, D. H. Seo, X. Ma, G. Ceder and K. Kang, *Adv. Energy Mater.*, 2012, **2**, 710-721.
2. X. Xu, W. Liu, Y. Kim and J. Cho, *Nano Today*, 2014, **9**, 604-630.
3. H. Hwang, H. Kim and J. Cho, *Nano Lett.*, 2011, **11**, 4826-4830.
4. K. Chang, D. Geng, X. Li, J. Yang, Y. Tang, M. Cai, R. Li and X. Sun, *Adv. Energy Mater.*, 2013, **3**, 839-844.
5. R. Chen, T. Zhao, W. Wu, F. Wu, L. Li, J. Qian, R. Xu, H. Wu, H. M. Albishri and A. S. Al-Bogami, *Nano Lett.*, 2014, **14**, 5899-5904.
6. J. w. Seo, J. t. Jang, S. w. Park, C. Kim, B. Park and J. Cheon, *Adv. Mater.*, 2008, **20**, 4269-4273.
7. H. S. Im, Y. J. Cho, Y. R. Lim, C. S. Jung, D. M. Jang, J. Park, F. Shojaei and H. S. Kang, *ACS Nano*, 2013, **7**, 11103-11111.
8. X. Huang, Z. Zeng and H. Zhang, *Chem. Soc. Rev.*, 2013, **42**, 1934-1946.
9. C. Tan and H. Zhang, *Chem. Soc. Rev.*, 2015, **44**, 2713-2731.
10. J. Zhou, J. Qin, X. Zhang, C. Shi, E. Liu, J. Li, N. Zhao and C. He, *ACS Nano*, 2015, **9**, 3837-3848.
11. L. Yang, S. Wang, J. Mao, J. Deng, Q. Gao, Y. Tang and O. G. Schmidt, *Adv. Mater.*, 2013, **25**, 1180-1184.
12. Z. Wang, T. Chen, W. Chen, K. Chang, L. Ma, G. Huang, D. Chen and J. Y. Lee, *J. Mater. Chem. A*, 2013, **1**, 2202-2210.
13. P. P. Wang, H. Sun, Y. Ji, W. Li and X. Wang, *Adv. Mater.*, 2014, **26**, 964-969.

14. S. Dutta, A. Bhaumik and K. C.-W. Wu, *Energy Environ. Sci.*, 2014, **7**, 3574-3592.

15. W. Qian, F. Sun, Y. Xu, L. Qiu, C. Liu, S. Wang and F. Yan, *Energy Environ. Sci.*, 2014, **7**, 379-386.

16. Y. Xia, Z. Xiao, X. Dou, H. Huang, X. Lu, R. Yan, Y. Gan, W. Zhu, J. Tu and W. Zhang, *ACS Nano*, 2013, **7**, 7083-7092.

17. X. Tao, J. Du, Y. Li, Y. Yang, Z. Fan, Y. Gan, H. Huang, W. Zhang, L. Dong and X. Li, *Adv. Energy Mater.*, 2011, **1**, 534-539.

18. X. Tao, L. Dong, X. Wang, W. Zhang, B. J. Nelson and X. Li, *Adv. Mater.*, 2010, **22**, 2055-2059.

19. J. Ryu, S. W. Kim, K. Kang and C. B. Park, *Adv. Mater.*, 2010, **22**, 5537-5541.

20. Y. Zhou, X. Rui, W. Sun, Z. Xu, Y. Zhou, W. J. Ng, Q. Yan and E. Fong, *ACS Nano*, 2015.

21. K. Y. Lee and D. J. Mooney, *Prog. Polym. Sci.*, 2012, **37**, 106-126.

22. M. Bruchet, N. L. Mendelson and A. Melman, *Processes*, 2013, **1**, 153-166.

23. Z. Schnepp, S. C. Wimbush, S. Mann and S. R. Hall, *CrystEngComm*, 2010, **12**, 1410-1415.

24. S. Leick, S. Henning, P. Degen, D. Suter and H. Rehage, *Phys. Chem. Chem. Phys.*, 2010, **12**, 2950-2958.

25. D. Kang, Q. Liu, J. Gu, Y. Su, W. Zhang and D. Zhang, *ACS Nano*, 2015.

26. R. Piñero, F. Leroux and F. Béguin, *Adv. Mater.*, 2006, **18**, 1877-1882.

27. D. Li, C. Lv, L. Liu, Y. Xia, X. She, S. Guo and D. Yang, *ACS Cent. Sci.*, 2015, **1**, 261-269.

28. R. Brayner, M.-J. Vaulay, F. Fiévet and T. Coradin, *Chem. Mater.*, 2007, **19**, 1190-1198.

29. Z. Schnepp, S. R. Hall, M. J. Hollamby and S. Mann, *Green Chem.*, 2011, **13**, 272-275.

30. K. Chang and W. Chen, *ACS Nano*, 2011, **5**, 4720-4728.

31. B. Zhang, X. Ye, W. Hou, Y. Zhao and Y. Xie, *J. Phys. Chem. B*, 2006, **110**, 8978-8985.

32. S. Xiong, B. Xi, D. Xu, C. Wang, X. Feng, H. Zhou and Y. Qian, *J. Phys. Chem. C*, 2007, **111**, 16761-16767.

33. J. Jiang, R. Yu, R. Yi, W. Qin, G. Qiu and X. Liu, *J. Alloys Compd.*, 2010, **493**, 529-534.

34. F. D. Han, Y. J. Bai, R. Liu, B. Yao, Y. X. Qi, N. Lun and J. X. Zhang, *Adv. Energy Mater.*, 2011, **1**, 798-801.

35. S. Zhuo, Y. Xu, W. Zhao, J. Zhang and B. Zhang, *Angew. Chem.*, 2013, **125**, 8764-8768.

36. C. Rao and A. Nag, *Eur. J. Inorg. Chem.*, **2010**, 4244-4250.

37. J. P. Paques, E. van der Linden, C. J. van Rijn and L. M. Sagis, *Adv. Colloid Interface Sci.*, 2014, **209**, 163-171.

38. C. P. Reis, R. J. Neufeld, S. Vilela, A. J. Ribeiro and F. Veiga, *J. Micro Cap.*, 2006, **23**, 245-257.

39. C. Y. Yu, L. H. Jia, B. C. Yin, X. Z. Zhang, S. X. Cheng and R. X. Zhuo, *J. Phys. Chem. C*, 2008, **112**, 16774-16778.

40. M. Boissière, P. J. Meadows, R. Brayner, C. Hélary, J. Livage and T. Coradin, *J. Mater. Chem.*, 2006, **16**, 1178-1182.

41. S. Wan, F. Guo, L. Shi, Y. Peng, X. Liu, Y. Zhang and Y. Qian, *J. Mater. Chem.*, 2004, **14**, 2489-2491.

42. M. Li, Q. Wu, M. Wen and J. Shi, , *Nanoscale Res. Lett.*, 2009, **4**, 1365-1370.

43. G. Diaz, R. Luna, D. R. Jara and L. Baños, *Cataly. Lett.*, 1990, **7**, 377-382.

44. Z. Li, Z. Xu, X. Tan, H. Wang, C. M. Holt, T. Stephenson, B. C. Olsen and D. Mitlin, *Energy Environ. Sci.*, 2013, **6**, 871-878.

45. M. S. Dresselhaus, G. Dresselhaus, R. Saito and A. Jorio, *Phys. Rep.*, 2005, **409**, 47-99.

46. R. Prins, V. De Beer and G. Somorjai, *Catal. Rev. Sci. Engin.*, 1989, **31**, 1-41.

47. M. J. Ledoux, A. Peter, E. A. Blekkan and F. Luck, *Appl. Catal. A*, 1995, **133**, 321-333.

48. J. Escobar, J. Toledo, M. Cortés, M. Mosqueira, V. Pérez, G. Ferrat, E. López-Salinas and E. Torres-García, *Catal. Today*, 2005, **106**, 222-226.

49. K. Chang and W. Chen, *Chem. Commun.*, 2011, **47**, 4252-4254.

50. K. Chang, W. Chen, L. Ma, H. Li, H. Li, F. Huang, Z. Xu, Q. Zhang and J.-Y. Lee, *J. Mater. Chem.*, 2011, **21**, 6251-6257.

51. Y. Miki, D. Nakazato, H. Ikuta, T. Uchida and M. Wakihara, *J. Power Sources*, 1995, **54**, 508-510.

52. S. Ding, D. Zhang, J. S. Chen and X. W. D. Lou, *Nanoscale*, 2012, **4**, 95-98.

53. J. Xiao, X. Wang, X. Q. Yang, S. Xun, G. Liu, P. K. Koech, J. Liu and J. P. Lemmon, *Adv. Funct. Mater.*, 2011, **21**, 2840-2846.

54. X. Fang, X. Guo, Y. Mao, C. Hua, L. Shen, Y. Hu, Z. Wang, F. Wu and L. Chen, *Chem. Asian J.*, 2012, **7**, 1013-1017.

55. F. L. Deepak, R. Esparza, B. Borges, X. L. Lozano and M. J. Yacaman, *ACS Catal.*, 2011, **1**, 537-543.

56. C. A. Fisher, V. M. Hart Prieto and M. S. Islam, *Chem. Mater.*, 2008, **20**, 5907-5915.

57. Y.-S. Lee, N. Kumada and M. Yoshio, *J. Power Sources*, 2001, **96**, 376-384.

58. A. Y. Shenouda and H. K. Liu, *J. Alloys Compd.*, 2009, **477**, 498-503.

59. M. Ren, Z. Zhou, Y. Li, X. Gao and J. Yan, *J. Power Sources*, 2006, **162**, 1357-1362.

60. K. Sato and H. K. Yoshida, *Japan. J. Applied Phys.*, 2001, **40**, L334.

61. R. Berenguer, J. M. Sieben, C. Quijada and E. Morallón, *ACS Appl. Mater. Interfaces*, 2014, **6**, 22778-22789.

62. J. Cabana, L. Monconduit, D. Larcher and M. R. Palacin, *Adv. Mater.*, 2010, **22**, E170-E192.

63. Y. Wang, J. Wu, Y. Tang, X. Lü, C. Yang, M. Qin, F. Huang, X. Li and X. Zhang, *ACS Appl. Mater. Interfaces*, 2012, **4**, 4246-4250.

64. G. Wang, S. Bewlay, J. Yao, H. Liu and S. Dou, *Electrochem. Solid State Lett.*, 2004, **7**, A321-A323.

65. H. Liu, D. Su, R. Zhou, B. Sun, G. Wang and S. Z. Qiao, *Adv. Energy Mater.*, 2012, **2**, 970-975.

66. K. Rui, Z. Wen, Y. Lu, J. Jin and C. Shen, *Adv. Energy Mater.*, 2014.

67. X. Ji, K. T. Lee and L. F. Nazar, *Nat. Mater.*, 2009, **8**, 500-506.

68. L. Zhang, H. B. Wu, Y. Yan, X. Wang and X. W. D. Lou, *Energy Environ. Sci.*, 2014, **7**, 3302-3306.

69. J. Zhou, J. Qin, X. Zhang, C. Shi, E. Liu, N. Zhao and C. He, *ACS Nano*, 2015.

70. Y. Liu, Y. Qiao, W. X. Zhang, Z. Li, X. L. Hu, L. X. Yuan and Y. H. Huang, *J. Mater. Chem.*, 2012, **22**, 24026-24033.

Graphic abstract：
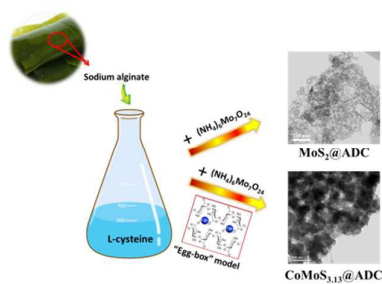
3D carbon supported metal sulfides were successfully synthesized through a facile, environment friendly and low cost alginate template strategy.